



Derivation of drag and lift force and torque coefficients for non-spherical particles in flows

Marian Zastawny, George Mallouppas, Fan Zhao, Berend van Wachem *

Division of Thermo fluids, Department of Mechanical Engineering, Imperial College London, Exhibition Road, London SW7 2AZ, UK

ARTICLE INFO

Article history:

Received 22 June 2011

Received in revised form 15 September 2011

Accepted 17 September 2011

Available online 5 October 2011

Keywords:

Non-spherical particles

Drag and lift coefficient

Torque coefficient

Turbulent gas–solid flow

Immersed boundary method

ABSTRACT

This paper derives and validates a new framework to predict the drag and lift coefficients as well as the torque coefficients for four non-spherical particle shapes in a flow with a wide range of flow Re and rotational Re numbers. Correlations are proposed for the drag force, the lift force, the pitching torque, and the torque caused by the rotation of the particle. Each of the correlations depends on Re number, the dimensionless rotation and the angle of incidence between the particle and the direction of the local fluid velocity. The fit parameters in the correlations for each of the particle shapes are determined by performing a large number of “true” DNS simulations of four different types of particles. The true DNS simulations are carried out with an improved mirroring immersed boundary method. The resulting correlations for the forces and the torques are suitable to be used in Eulerian–Lagrangian simulations, where an accurate prediction of the forces and torques is required to determine the motion of the particles.

© 2011 Elsevier Ltd. All rights reserved.

1. Introduction

The ability to predict the behaviour of turbulent gas–solid flows is vital for the successful design and determination of optimum operating conditions of numerous industrial applications, e.g. cyclone separators, fluidised beds, dust collectors, and pulverised-coal combustors to name a few. The dynamics of these type of systems can be investigated through experiments or through numerical simulations. The low cost and large amount of data and insight that can be obtained make the numerical approach very convenient option. Still, performing large scale numerical study of complex multiphase flow requires some assumptions and empirical data describing the interactions between the fluid and the particles.

So far, nearly all studies performed on the gas–particle flows model particles as perfect spheres. This assumption is very convenient due to its simplicity, the fact that the behaviour of spheres is well known, and the availability of a number of models to describe the interaction with fluid flow. Dependence of the drag coefficient of a sphere on the Reynolds number can be found for example in Schiller and Naumann (1933). Also behaviour of rotating spheres and spheres moving in a shear flow have been studied with additional correlations for Magnus and Saffman forces available in Niazmand and Renksizbulut (2003), Kurose (1999), and Dennis et al. (1980).

Nevertheless, a vast number of the applications deals with non-spherical particles, which makes analysis of these type of flows more complicated. Spheres can be described by a single characteristic value, i.e. the diameter, whereas non-spherical particles require more parameters. Even very regular shapes, like ellipsoids or fibres, are described by at least two parameters. Moreover, the particles can have varying orientation with respect to the flow, what additionally complicates the description of their behaviour. Besides the drag force, a non-spherical particle also experiences a transverse lift force along with pitching and rotational torques.

Even though most of the papers on gas–solid flows focus on spherical particles, the effects of non-sphericity had been addressed by some researchers. In order to account for the deviation from the idealised spherical shape, a so-called “sphericity factor”, Φ , has been introduced (Wadell, 1934; Kunii and Levenspiel, 1991). Sphericity is defined as the ratio of the surface area of a sphere with equal volume as the non-spherical particle over the surface area of the non-spherical particle. By definition, the sphericity factor is less than or equal to one, where one corresponds with a sphere. In most engineering handbooks (e.g. Crowe, 2006) the drag of a non-spherical particle is estimated by using correlations for spherical particles and modified to take into account the sphericity factor.

Using sphericity to describe non-spherical particles may give promising results, nonetheless it is far from ideal. For instance, the same value of sphericity can be obtained for a needle like prolate ellipsoid and for a disc, while their behaviour in the flow will be different. Moreover, the sphericity does not account for the orientation of the non-spherical particle. In order to introduce

* Corresponding author. Tel.: +44 20 759 47030; fax: +44 20 759 45702.

E-mail address: B.van-Wachem@imperial.ac.uk (B. van Wachem).

orientation dependency in drag correlations, some researchers, like Hölzer and Sommerfeld (2008), use two additional factors: the sphericity determined in the lengthwise direction and one in the crosswise direction, making the effective sphericity orientation dependent.

Other ways to describe the shape of the particle are proposed by Rosendahl (2000) or by Loth (2008a). Rosendahl uses the super-elliptic function to describe the particle shape and to predict the drag at two extreme orientations, i.e. aligned with the flow, and at 90° relative to incoming fluid velocity. On the other hand Loth describes the particle by its aspect ratio, which is applied to calculate shape correction factors both in parallel and cross-wise directions. The effects of orientation can be also included by modifying the reference area in force coefficient expressions. The most complete overview of the existing methods for analysing non-spherical particles can be found in a paper by Mando and Rosendahl (2010). So far, the majority of the research has been focused on determining the drag coefficient, while the secondary motion resulting from the lift and torques has received very little attention.

The current paper shows the results of direct numerical simulations of the flows past four different non-spherical particles presented in Table 1. The obtained forces are then used to design shape-specific correlations, that describe the interactions between the fluid and the particles. The equations can be used as a base of large scale analysis of complex flows with non-spherical particles.

2. Forces on particles

Few closed models describing the motion of a non-spherical particle in the fluid are available. In a Lagrangian framework the translation motion of particles can be described by Newtonian equations of motion (Yin et al., 2003):

$$m_p \frac{D\vec{v}_p}{Dt} = \vec{F}_D + V_p(\rho_p - \rho_f)\vec{g} + \vec{F}_{PG} + \vec{F}_{VM} + \vec{F}_L \quad (1)$$

where m_p is the particle mass, V_p is the particle volume, ρ_p is the particle density, ρ_f is the fluid density, and \vec{v}_p is the translational velocity of the particle centre of mass. The forces acting on the particle are given on the right hand side of the equation and correspond to drag, buoyancy, the force due to the fluid pressure gradient, the virtual mass force and the lift force. For heavy particles in dilute suspensions the drag, lift and inertia effects play dominant role in determining the motion of the particle (Lazaro and Lasheras, 1989), therefore these forces are the main focus of the current paper.

When describing rotational motion of an axisymmetric particle, it is convenient to use an additional coordinate system, fixed at the particle centre and aligned with the axis-symmetric axis of the particle. In such system the equations of motion take the following form (Yin et al., 2003):

$$I_{x'} \frac{d\omega_{x'}}{dt} - \omega_{y'}\omega_{z'}(I_{y'} - I_{z'}) = T_{x'} \quad (2)$$

$$I_{y'} \frac{d\omega_{y'}}{dt} - \omega_{z'}\omega_{x'}(I_{z'} - I_{x'}) = T_{y'} \quad (3)$$

$$I_{z'} \frac{d\omega_{z'}}{dt} - \omega_{x'}\omega_{y'}(I_{x'} - I_{y'}) = T_{z'} \quad (4)$$

where $I_{x'}$, $I_{y'}$, $I_{z'}$ are the moments of inertia; $\omega_{x'}$, $\omega_{y'}$, $\omega_{z'}$, the angular velocities, while $T_{x'}$, $T_{y'}$, $T_{z'}$ are the torques with respect to particle axes. It is clear that for a successful model of particle motion one needs to know the drag and lift forces along with the torques acting on the particle in various flow conditions.

There are few research papers concerning the analytical derivation of the flow past ellipsoids at very low Reynolds numbers. Brenner (1963) established an expression for the forces acting on the prolate ellipsoids in a flow, while Jeffery (1922) introduced the equations for the torques on the particle. These models have been applied in various analysis of flows with non-spherical particles, (e.g. Gallily and Cohen, 1979; Marchioli et al., 2010; Mortensen et al., 2008). The aforementioned models have, however, limited use in the cases of flows where particle Reynolds numbers are larger than unity. Therefore, an alternative approach is necessary in order to calculate the forces on the particle over a wider range of Re . The most suitable way is to perform an experimental study or numerical analysis to obtain the forces and torques on particles over a range of flow conditions.

In order to predict the fluid interaction with a general non-spherical particle, simulations over a range of Reynolds numbers and over the range of the two independent Euler angles, ranging from 0° to 360° and 0° to 180° respectively, are to be performed. This leads to a very large number of required simulations. However, many non-spherical shapes can be assumed axis-symmetric and modelled as prolate or oblate ellipsoids or as cylindrical fibres. For these shapes, by a rotation of coordinate system, any three-dimensional arrangement with the flow field can be converted into simplified 2D flow case as illustrated in Fig. 1.

This significantly simplifies the problem and allows to minimize the number of parameters needed to perform a full study of the particle behaviour. In a two-dimensional coordinate system the particle experiences a drag force acting in the direction of the flow, a transverse lift force, a pitching torque and torque counteracting the rotation. Details on these forces and the current state of knowledge are described below.

2.1. Drag force

The drag force experienced by a non-spherical particle acts in the direction of the flow velocity and is characterised by the drag coefficient, defined as:

Table 1
The overview of the four non-spherical particles considered in this paper.

Shape	Parameters	Shape	Parameters
Ellipsoid 1	$\Phi = 0.88$ $\frac{a}{b} = \frac{5}{2}$	Ellipsoid 2	$\Phi = 0.99$ $\frac{a}{b} = \frac{5}{4}$
Disc	$\Phi = 0.88$ $\frac{a}{b} = \frac{5}{1}$	Fibre	$\Phi = 0.99$ $\frac{a}{b} = \frac{5}{1}$

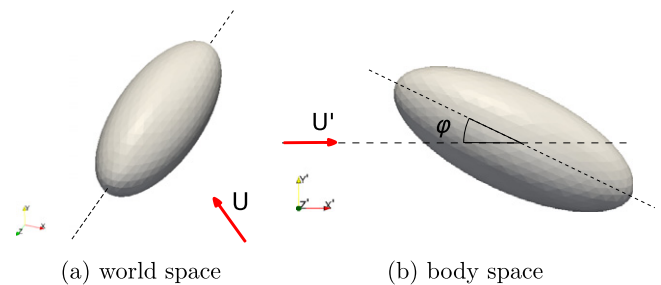


Fig. 1. The fluid velocity in world space (left) and in body space (right). The angle of incidence is defined as the angle between the direction of the fluid velocity and the longest axis of the body.

$$C_D = \frac{F_D}{\frac{1}{2} \rho \tilde{u}^2 A_p} \quad (5)$$

where F_D is the actual drag force, $\tilde{u} = u_\infty - u_p$ is the velocity of the particle relative to the local undisturbed fluid velocity u_∞ , ρ is the fluid density, and $A_p = \frac{\pi}{4} d_p^2$ the reference area with d_p being the equivalent particle diameter, i.e. the diameter of a sphere with the same volume as the considered particle. The choice of the definition of the reference area is arbitrary, as long as it is used consistently. Defining the reference area as the cross-sectional area of volume equivalent sphere guarantees that it stays constant regardless of the angle of incidence. It also allows to easily compare the coefficient for various shapes and orientations.

The drag coefficient for non-spherical particles has been focus of research for some time. Similarly as in the case of spherical particles, the drag coefficient is determined empirically for particle Reynolds numbers ($Re = \frac{\rho \tilde{u} d_p}{\mu}$) larger than unity; this can be done experimentally (e.g. Wen and Yu, 1966; Ergun, 1952) or computationally (e.g. Loth, 2008b; Hölzer and Sommerfeld, 2009). Haider and Levenspiel (1989) correlate the experimentally obtained drag force for a number of particle shapes and particle Reynolds numbers using the sphericity coefficient. Hölzer and Sommerfeld (2008) propose an improvement to the prediction by introducing crosswise sphericity factor Φ_L , which is the ratio of the crosswise area of the equivalent sphere to the crosswise area of the particle. Loth (2008b), on the other hand, uses shape correction factors based on the particle aspect ratio to determine the drag in the Stokes and Newton flow regimes, while the drag in the intermediate Re region is calculated by matching the drag coefficients from the two regimes. A different approach is suggested by Rosendahl (2000), who introduces a formula based on several correction factors using the super-elliptic description of the shape of the non-spherical particle. There are also a number of other correlations which have been proposed on similar grounds (e.g. Hartman et al., 1994; Ganser, 1993; Loth, 2008a), and a review can be found in Chhabra et al. (1999). Although all of these correlations are complex and contain 5–10 fit parameters, the errors in their prediction is still quite large; a typical mean error of 25%, with maximal errors exceeding 100% (Hölzer and Sommerfeld, 2008; Chhabra et al., 1999).

It is worth noting that only few of the available correlations predict the change of the drag coefficient with the relative angle of the particle to the flow velocity, sometimes referred to as the angle of incidence. Rosendahl (2000) heuristically suggests to correlate the drag coefficient with this angle using the following equation:

$$C_D(\varphi) = C_D(0^\circ) + (C_D(90^\circ) - C_D(0^\circ)) \sin^3 \varphi \quad (6)$$

where φ is the angle of incidence. In other approaches the angle dependency is obtained by modifying the sphericity or the drag coefficient definition itself, taking into account the changing crosswise area of the particle.

2.2. Lift force

Lift force on a particle not aligned with the flow velocity is a result of non-axisymmetric flow field. It acts in the direction perpendicular to the fluid velocity and similarly as the drag can be characterised by lift coefficient, defined as:

$$C_L = \frac{F_L}{\frac{1}{2} \rho \tilde{u}^2 \frac{\pi}{4} d_p^2} \quad (7)$$

where F_L is the actual lift force—the fluid force acting orthogonal to the flow velocity.

Compared to the drag force, significantly less research work has been done to predict the lift exerted on a non-spherical particle by

the fluid motion. There is some work on deriving equations for the lift coefficients for rotating spherical particles, or spheres in a shear flow (e.g. Rubinow and Keller, 1961; Cherukat et al., 1999), but as the transverse forces in case of non-spherical particles are a product of different sources, the aforementioned studies are of a limited usage. A common assumption for the lift force, is that it is proportional to the drag force with the orientation of the non-spherical particle, by the so called “cross flow principle” (Hoerner, 1965),

$$\frac{C_L}{C_D} = \sin^2 \varphi \cos \varphi \quad (8)$$

There is an attempt to improve this equation by Mando and Rosendahl (2010), introducing a dependency on Reynolds number, however this equation does not enhance the quality of the prediction.

2.3. Pitching torque

Since the centre of pressure of the total aerodynamic force acting on the particle does not coincide with the particle's centre of mass, a pitching torque is generated. It acts around the axis perpendicular to the plane where the forces are present and attempts to increase the particle's angle of incidence. Analogously as the force coefficients, the torque coefficient is defined as:

$$C_T = \frac{T_p}{\frac{1}{2} \rho \tilde{u}^2 \frac{\pi}{8} d_p^3} \quad (9)$$

where T_p is the pitching torque. Note the d_p^3 term in the denominator, instead of d_p^2 present for force coefficients.

An heuristic expression for the torque for low Reynolds number on a non-spherical particle is proposed in Besnard and Harlow (1986). This expression originates from the limits of the lift force, its invariance under a 180° rotation of the particle and that it should vanish if the angle is 90°. This expression is employed by Rosendahl (2000) to predict the behaviour of non-spherical particles in a swirling flow. This expression has, however, not been rigorously validated before. Other approaches include determining the centre of pressure on the particle as a function of angle of incidence and determining the resulting torque as the cross-product of the total force and the distance between the centre of gravity and the centre of pressure (Mando and Rosendahl, 2010).

2.4. Rotational torque

A particle can gain rotation due to the pitching torque or by collisions with the walls or other particles. The rotation of a non-spherical particle can occur in two modes: around the axis of symmetry and around the axis perpendicular to the axis of symmetry. In both cases the rotational torque can be characterised by the torque coefficient defined as:

$$C_R = \frac{T_R}{\frac{1}{2} \rho \left(\frac{d_p}{2}\right)^5 |\Omega|} \quad (10)$$

where T_R is the rotational torque, $\vec{\Omega} = \frac{1}{2} \nabla \times \vec{u} - \vec{\omega}_p$ is the relative rotation with $\vec{\omega}_p$ being the particle angular velocity. The rotational torque coefficient is different for every mode of rotation.

There is no easily available correlation describing the rotational torque of a non-spherical particle. The closest useful assumption is the formula for spheres, suggested by Dennis et al. (1980), where the coefficient depends on rotational Reynolds number, which is defined as:

$$Re_R = \frac{\rho d_p^2 |\vec{\Omega}|}{\mu} \quad (11)$$

Some study on the secondary motion of the particle has been done. Lattice Boltzmann simulations were performed in Hölzer and Sommerfeld (2009) for various shapes and graphs of the obtained lift and torque coefficients are shown. However, no empirical correlations are presented.

Summarising, even though there exists a number of correlations allowing for calculation of forces on an arbitrary non-spherical particle, they have limited accuracy for an arbitrary particle. Therefore in this research work the drag, lift and torque coefficients are determined for each particle type. To determine the forces and torque on a non-spherical particle as a function of Reynolds number and particle orientation, a large number of true DNS simulations are performed, where an accurate flow field around the particle is determined. The term “true” emphasizes that not only all the flow scales are resolved but also a no-slip boundary condition is applied at the surface of particle. The forces which are obtained from the true DNS are coarse-grained into semi-empirical models predicting the drag, lift and pitching torque coefficients as a function of particle Reynolds number and orientation, expressed by the angle of incidence. Additionally the rotational torque coefficients for different modes of rotation are determined as a function of rotational Reynolds number Re_R .

3. Numerical framework

Because of the large number of simulations required, a computationally effective and efficient framework is desired to deal with flows including non-spherical particles. Moreover, the framework should be able to handle rotating particles. Throughout the years, various methods coupling the particles with surrounding fluid have been developed. Among the oldest ones is the arbitrary-Lagrangian–Eulerian method (Hu, 1996), where a two-dimensional unstructured grid is created around the bodies and the mesh is adapted as they move. Although this method works very well when the deformations are small, like in aerodynamic problems, the necessity to create a new mesh every time step if the deformations are large is time consuming and may limit accuracy.

The immersed boundary (IB) method tackles this problem by using Cartesian grid for the fluid, while the presence of particles is accounted for by modifying flow variables where the IB crosses the Eulerian mesh cells. Peskin (1977) was among the first to propose the IB method. In this implementation, the coupling between the phases is achieved by calculating point forces representing the influence of the boundaries. The forces are distributed over the mesh using a distribution function. This method is first order accurate in space and time. The reason for this is that a blurred representation of the boundary is achieved.

An alternative way to implement the IB method, sometimes called immersed interface method, is to apply the boundary conditions directly at the interface of the particle. It is introduced in Mohd-Yusof (1997), where a smooth velocity gradient is applied over the IB. Despite being able to achieve some promising results, the method exhibits problems with mass conservation in the boundary cells. Therefore, this work employs an improved type of IB method from Mohd-Yusof (1997), the mirroring immersed boundary method.

3.1. Implicit mirroring immersed boundary method

This work outlined in this paper employs the implicit mirroring immersed boundary (MIB) method to resolve the flow surrounding the analysed particles. The first ideas on this method are introduced in Mark and van Wachem (2008), although a number of improvements have been made (van Wachem et al., 2010). Due to the fact that it uses a non-boundary conforming grid, it is

capable to resolve detailed flow around an arbitrary non-spherical particle. The surface of the particle is triangulated and an immersed boundary condition is applied at the cells where the particle surface triangles intersect the fluid Eulerian grid. The MIB method mirrors the velocity field through the surface triangles by adding a constraint to the Navier–Stokes equations and creating a fictitious flow inside the particle. This is done by setting a fictitious exterior normal point \vec{x}_e , as depicted in Fig. 2. The mirrored point is defined as the \vec{x}_{iib} is mirrored along the normal of its closest interface surface triangle. Hence, the smallest distance between the interface and the fictitious point, \vec{x}_e , is equal:

$$\vec{x}_e = \vec{x}_{iib} + 2\vec{dn} \quad (12)$$

where \vec{dn} is the normal distance from the \vec{x}_{iib} to the closest interface triangle.

If the exterior normal point coincides with a discrete velocity point, the Dirichlet condition for the velocity of the \vec{x}_{iib} point is trivial. More generally, the exterior normal point lies between the discrete velocity points and therefore the velocity needs to be implicitly interpolated using the surrounding points. The mirrored velocity is set to the reversed interpolated velocity plus the boundary velocity. The interior velocities are set to the boundary (IB) velocity. In order to conserve mass, the velocity of the mirrored points \vec{x}_{iib} is excluded from the continuity equation. The method has been shown to be second order accurate in predicting the drag, lift and torque forces on a rotating sphere (van Wachem et al., 2010).

3.2. Calculation of the forces

The force on the immersed particle is indirectly given by the numerical framework, as the solution of the Navier–Stokes equations implicitly accounts for the presence of the boundary of the

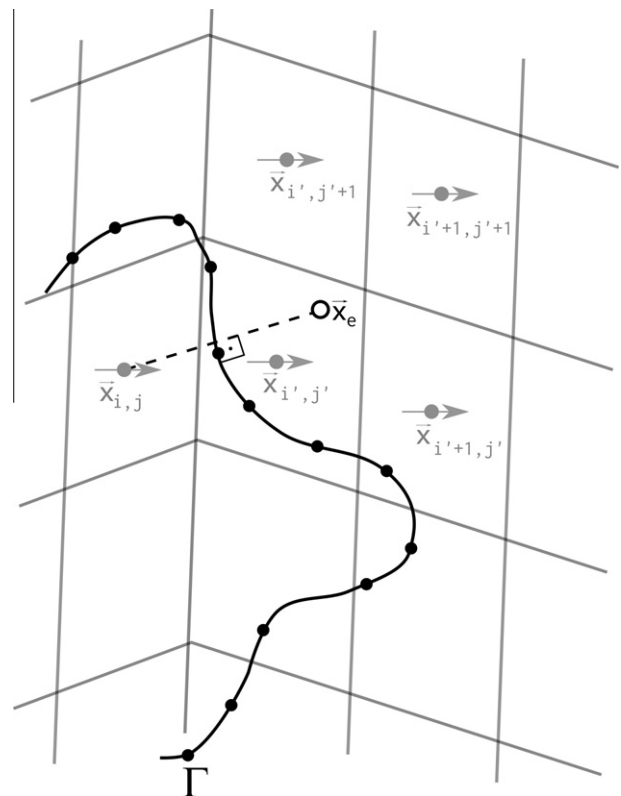


Fig. 2. A two-dimensional representation of the MIB method, the exterior normal point \vec{x}_e with its surrounding interpolation points.

non-spherical particle. The total force consists of two distinctive contributions, i.e. the pressure and the viscous forces. These forces are integrated over the interface Γ , giving

$$F_i = \int_{\Gamma} (-p\delta_{ij} + \tau_{ij})n_j dS \quad (13)$$

Neither the pressure nor the velocity derivatives, required to determine the surface forces, are explicitly known at the interface and therefore need to be determined from the resolved flow field. To determine the pressure at the interface, three auxiliary points, normal to the considered triangle, are applied to extrapolate the value of the pressure onto the surface. Their position with respect to the fluid mesh is shown in Fig. 3. The pressure on the surface is found with second order accuracy according to the approximation:

$$p_{\vec{x}_c} \approx p_{\vec{x}'} + \Delta \left(\frac{\partial p}{\partial \vec{x}} \right)_{\vec{x}'} \approx \frac{1}{2} (5p_{\vec{x}'} - 4p_{\vec{x}''} + p_{\vec{x}'''}) \quad (14)$$

The viscous force component, on the other hand, depends on the velocity gradients, which are evaluated at the surface. This can be written by Taylor series expansion as:

$$u_i(\vec{x}_c) = u_i(\vec{x}_{nb}) + \left(\frac{\partial u_i}{\partial x_j} \right)_{\vec{x}_c} (\vec{x}_{nb} - \vec{x}_c) + O(\vec{x}_{nb} - \vec{x}_c)^2 \quad (15)$$

where $u_i(\vec{x}_c)$ is the velocity at the triangle centre, $u_i(\vec{x}_{nb})$, are the fluid velocities of neighbouring cells, $(\vec{x}_{nb} - \vec{x}_c)$ is the distance from triangle centre to the neighbouring cell and $\left(\frac{\partial u_i}{\partial x_j} \right)_{\vec{x}_c}$ is the sought velocity gradient at the surface. To obtain the most accurate representation of the gradients, a weighted least square problem is solved, where the velocities are based on 17 neighbouring cells, as shown in Fig. 4. The velocity on the surface, $u_i(\vec{x}_c)$, is obtained by interpolation, similarly as in the case of the \vec{x}_e mirroring and pressure points.

4. Simulation set-up

A true direct numerical simulation (DNS) framework has been used to determine the drag, lift and torque of the bodies shown in Table 1. A triangulated representation of the bodies is introduced in a domain with size $20d_p \times 20d_p \times 10d_p$ for low Reynolds number $Re < 1$ and a cubical domain $10d_p \times 10d_p \times 10d_p$ for high Re number simulations. The set-up is illustrated in Fig. 5.

A uniform flow with the velocity $U_{\infty} = 1.0$ m/s is set along the positive x axis. The fluid density is $\rho = 1$ kg/m³. A full slip (i.e. no velocity gradient) boundary condition is applied on the boundaries

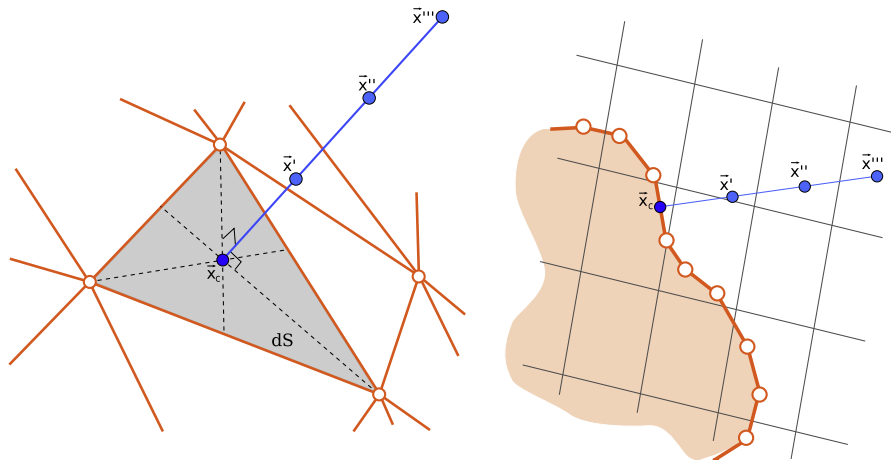


Fig. 3. An illustration of the points used to extrapolate the pressure onto the particle surface and their position relatively to the fluid cells. Three-dimensional representation is shown on the left, while a two-dimensional projection is illustrated on the right hand side.



Fig. 4. A two-dimensional view of neighbouring cells which are used to reconstruct the velocity gradient. Note that the IB points far inside the particle are not included in the velocity gradient determination, as they are forced to match the velocity of the particle and do not represent the fluid.

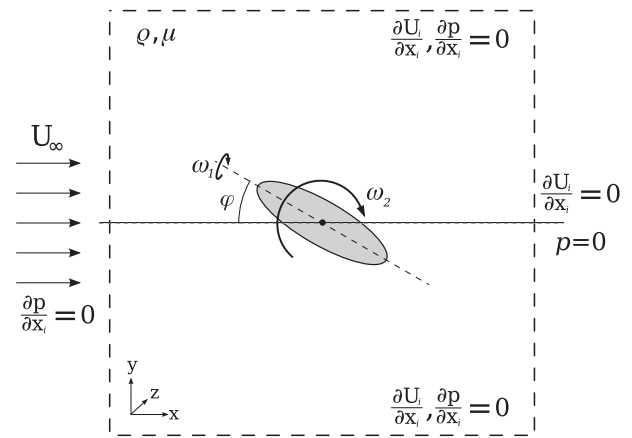


Fig. 5. A schematic of the fluid domain used for analysis along with the boundary conditions applied at the walls.

of the domain. The pressure is set to P_{out} at the outlet, and zero gradient in pressure is specified on other boundaries of the domain. The simulations are initially resolved using upwind scheme with very large time step in order to get the first approximation of the

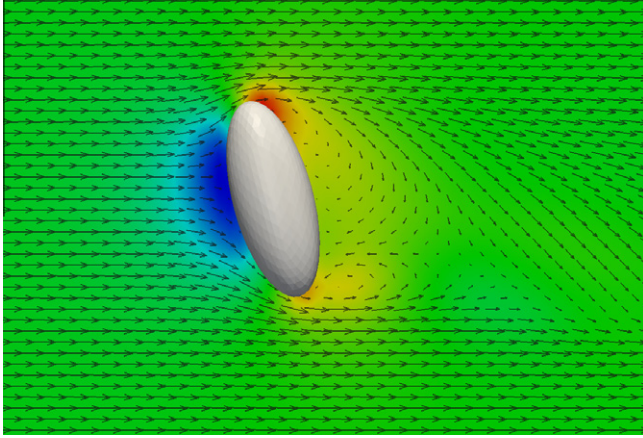


Fig. 6. A snapshot of the velocity (arrows) and pressure field (colour) in a flow past ellipsoid 1 at $Re = 200$ and $\varphi = 70^\circ$. (For interpretation of the references to colour in this figure legend, the reader is referred to the web version of this article.)

flow field. Afterwards the time step is decreased to maintain the $CFL < 1$ condition and the discretisation scheme is changed to central for increased accuracy.

The number of mesh cells in the domain depends on the Reynolds number and varies between 8 and 12 cells on the diameter

of equivalent sphere. The particle Reynolds number, Re , based upon the equivalent particle diameter, d_p , is varied between 0.1 and 300 by adjusting the fluid viscosity μ . Simulations at different particle angles of incidence φ ranging from 0° to 90° are performed. The particle is fixed and does not rotate. The mirroring immersed boundary is used to enforce the no-slip boundary condition on the surface of the particle and calculate the forces on the non-spherical particle. Obtained force values are applied to establish particle specific empirical relations for force coefficient as a function of Re and φ .

Additionally a number of simulations with rotating particle is performed. The particle can rotate around its axis of symmetry (mode 1) or around perpendicular plane (mode 2). In rotational analysis the fluid is stationary, while the rotational Reynolds number Re_R is determined by adjusting angular velocity (ω_1 or ω_2) of the particle or the viscosity of the fluid μ .

5. Results and discussion

True DNS of the flow past each particle type is performed in order to obtain shape-specific drag, lift and torque characteristics as a function of Reynolds number and angle of incidence. The flow is calculated with enforcing a no-slip boundary condition at the particle surface by the mirroring immersed boundary condition presented in Section 3. The length of simulations allows to obtain

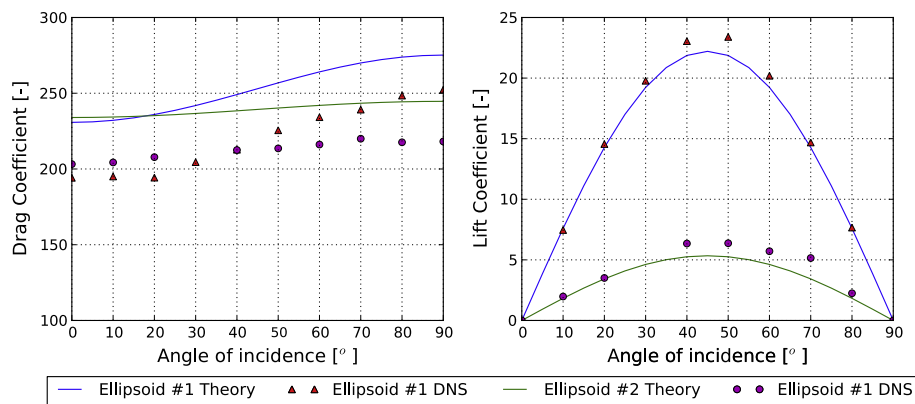


Fig. 7. The comparison of the values for drag and lift coefficients obtained from Brenner (1963) and Gallily and Cohen (1979) with the current DNS results for prolate ellipsoids at $Re_p = 0.1$.

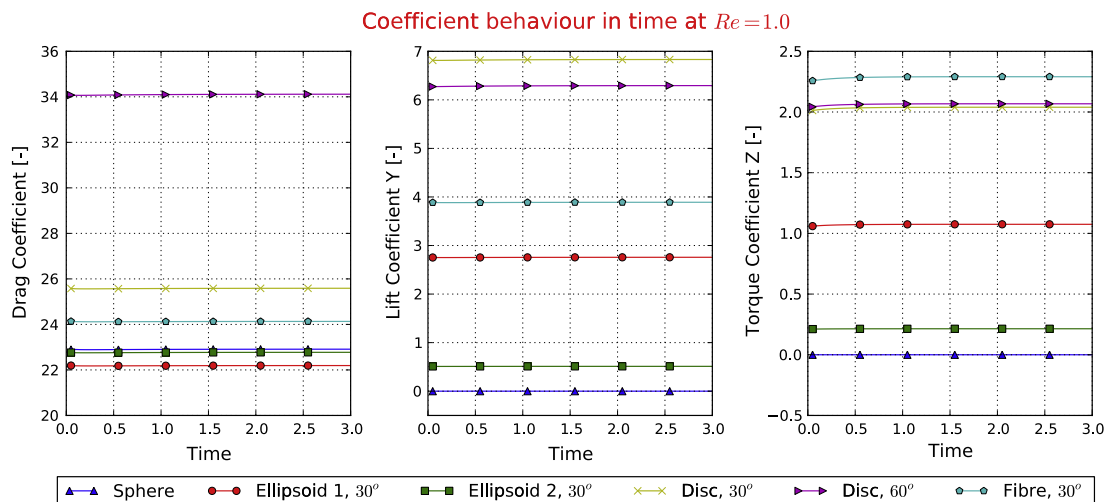


Fig. 8. The force coefficients and torque coefficients as a function of time for the different particles with flow at $Re = 1$.

steady state solution for low Re or constant averages in case of unstable flows. A sample result is illustrated in Fig. 6, which shows an instantaneous flow field around the ellipsoid 1 at $Re = 200$.

Obtained values for force coefficients at low Reynolds numbers are compared to the models presented in Brenner (1963) and Gallily and Cohen (1979). This comparison is shown in Fig. 7, where a reasonable agreement between the results is seen. The difference in the calculated drag coefficient results from the effects of the finite domain on the current simulations and the non-zero Re number. It is however worth noting that the results deviate quickly from each other as the Reynolds number increases. The comparison with the torque formulas given in Jeffery (1922) is not suitable, as this model applies only in the case of flows with gradients in incoming velocity, what is not the case in the current research.

Fig. 8 shows the behaviour of the force coefficients as the time progresses in simulations at low Reynolds number. After the fast readjustment of values of the coefficients, resulting from the change of discretisation scheme, constant coefficients are instantly achieved. The difference in coefficient values for various particles can also be clearly seen. For higher Reynolds numbers, e.g. $Re = 300$, the flow behaviour sometimes becomes oscillatory, as illustrated in Fig. 9. It is worth noting that the oscillations in the flow are more visible when looking at the lift or torque coefficients than the drag. In steady flows, the small fluctuations of the force coefficients tend to be damped, as seen in the case of the fibre in the figure. However, in some cases the perturbations may grow and a transition to an unsteady mode will occur. The unsteady motion can be of nearly periodic or chaotic character. It should be noted that both the shape and the angle of incidence of the non-spherical particle play key role in the resulting flow behaviour, changing the value of the Reynolds number at which the transition occurs. In the current work the forces used for determining the correlations describing the coefficients are obtained by averaging the coefficients throughout the simulation after the initial period of time, allowing for readjustment to a new discretisation scheme.

5.1. Drag

For each particle shape, true DNS simulations are done at various Re numbers, rotational Re numbers and various angles of incidence between the particle and the direction of mean flow. For each simulation, force and torque coefficient values are obtained.

The obtained coefficient values are used to create shape-specific force correlations as functions of the Reynolds numbers and the angle of incidence φ . In this paper we propose a new framework for the force coefficients, which leads to excellent fits for all of the simulated particle shapes, fluid flows, and rotations. The proposed equation for the drag coefficient is

$$C_D(\varphi) = C_{D,\varphi=0^\circ} + (C_{D,\varphi=90^\circ} - C_{D,\varphi=0^\circ}) \sin^{a_0} \varphi \quad (16)$$

where

$$C_{D,\varphi=0^\circ} = \frac{a_1}{Re^{a_2}} + \frac{a_3}{Re^{a_4}} \quad (17)$$

$$C_{D,\varphi=90^\circ} = \frac{a_5}{Re^{a_6}} + \frac{a_7}{Re^{a_8}} \quad (18)$$

The resulting particle-specific values of the fit parameters obtained from the simulations are listed in Table 2. The dependency of the drag coefficient on the Reynolds number is shown in Fig. 10. The drag coefficient decreases with the Reynolds number for all particle types. A considerable difference between various shapes can be observed. It is also worth noting the change between drag coefficients of the ellipsoid 1 at two extreme orientations. The ratio between the lowest and the highest drag coefficient grows as the Re is increased. Similar observations can be made for other types of particles.

The obtained results are compared with the expressions for drag found in (Mando and Rosendahl, 2010; Hölzer and Sommerfeld, 2008):

Table 2

The values of fit parameters for equation for the drag coefficient (Eq. (18)) resulting from the DNS simulations of analysed particles.

Coefficient	Ellipsoid 1	Ellipsoid 2	Disc	Fibre
a_0	2.0	1.95	1.96	2.12
a_1	5.1	18.12	5.82	20.35
a_2	0.48	1.023	0.44	0.98
a_3	15.52	4.26	15.56	2.77
a_4	1.05	0.384	1.068	0.396
a_5	24.68	21.52	35.41	29.14
a_6	0.98	0.99	0.96	0.97
a_7	3.19	2.86	3.63	3.66
a_8	0.21	0.26	0.05	0.16

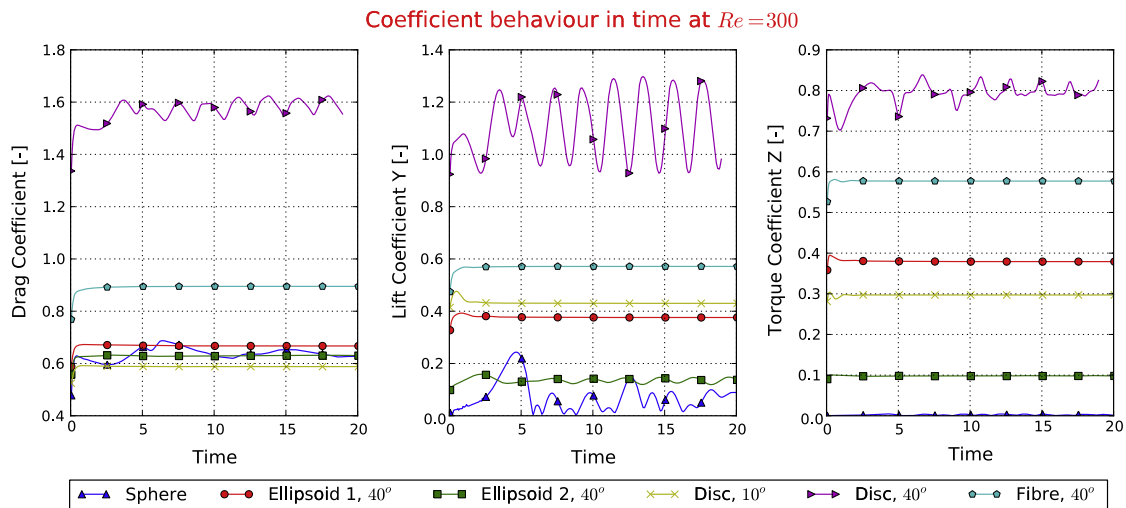


Fig. 9. The force coefficients and torque coefficients as a function of time for the different particles with flow at $Re = 300$. The sphere is in the unsteady periodic flow regime, giving rise to an additional transverse lift force. Flow past a disc at 10° is steady, however large oscillations are present at 40° . On the other hand, the flow remains steady even at 40° for the fibre and ellipsoid 1, whereas for a nearly spherical ellipsoid 2 small oscillations are present in the lift coefficient.

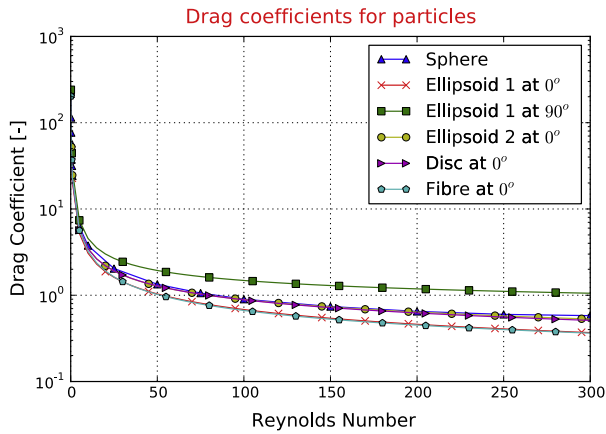


Fig. 10. Drag coefficients for the analysed shapes as a function of Reynolds number.

$$C_D(\varphi) = C_{D,\varphi=0^\circ} + (C_{D,\varphi=90^\circ} - C_{D,\varphi=0^\circ}) \sin^3(\varphi) \quad (19)$$

$$C_{D,\varphi=0.90} = \frac{8}{Re} \frac{1}{\sqrt{\Phi_\perp}} + \frac{16}{Re} \frac{1}{\sqrt{\Phi}} + \frac{3}{\sqrt{Re}} \frac{1}{\Phi^{0.75}} + 0.4210^{0.4(-\log \Phi)^{0.2}} \times \frac{1}{\Phi_\perp} \quad (20)$$

Fig. 11 presents the dependence of the drag coefficient values on the angle of incidence for different particles. The coefficient grows with increasing angle following an “s” shaped curve. The angle dependence has much higher influence for large Reynolds numbers, as the $C_{D,max}/C_{D,min}$ ratio increases. The equation proposed by

Hölzer and Sommerfeld (2008) shows generally good agreement with the current results, however it tends to under-predict the influence of orientation as well as over-predict the drag for particles aligned with the flow at low Reynolds numbers.

5.2. Lift

Because of the large amount of results, the lift experienced by the particle is correlated with the Reynolds number and the angle of incidence, φ . Usually, in literature, lift is directly correlated with drag as in Eq. (8). However the current results show that this approach does not seem appropriate as the relation of the lift coefficient to drag is more irregular than that of the lift coefficient alone.

The new equation for the lift coefficient proposed in this article is

$$C_L = \left(\frac{b_1}{Re^{b_2}} + \frac{b_3}{Re^{b_4}} \right) \sin(\varphi)^{b_5+b_6 Re^{b_7}} \cos(\varphi)^{b_8+b_9 Re^{b_{10}}} \quad (21)$$

The first term describes the magnitude of the coefficient while the powers of the trigonometric functions characterise the varying dependence on the angle. As with the newly proposed equation for the drag coefficient, the above equation for the lift gives a very good fit for all of the particle shapes, Reynolds numbers and incident angles. The parameters resulting from fitting the simulations are given in Table 3.

The calculated lift is compared with literature lift related to the drag by the “cross-flow” principle given in Eq. (8). The lift coefficient behaviour at various orientations is illustrated in Fig. 12. The lift curve is not exactly symmetric with the highest values

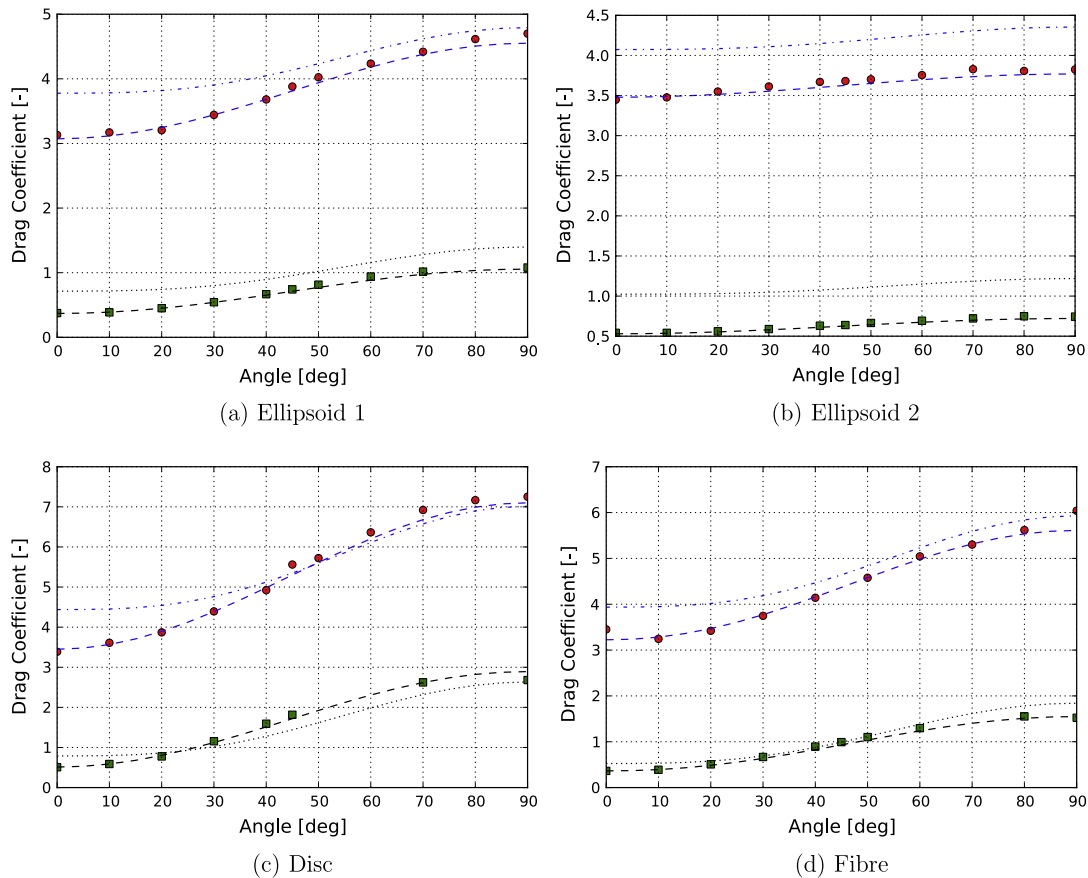


Fig. 11. Drag coefficients of particles as a function of angle of incidence. (○) Simulation at $Re = 10$; (—) present correlation (Eq. (18)) at $Re = 10$; (---) correlation of Hölzer and Sommerfeld (2008) at $Re = 10$; (□) simulation at $Re = 300$; (---) present correlation (Eq. (18)) at $Re = 300$; (---) correlation of Hölzer and Sommerfeld (2008) at $Re = 300$. (For interpretation of the references to colour in this figure legend, the reader is referred to the web version of this article.)

Table 3

The values of fit parameters for equation for the lift coefficient (Eq. (21)) resulting from the DNS simulations of analysed particles.

Coefficient	Ellipsoid 1	Ellipsoid 2	Disc	Fibre
b_1	6.079	0.083	12.111	8.652
b_2	0.898	−0.21	1.036	0.815
b_3	0.704	1.582	3.887	0.407
b_4	−0.028	0.851	0.109	−0.197
b_5	1.067	1.842	0.812	0.978
b_6	0.0025	−0.802	0.249	0.036
b_7	0.818	−0.006	−0.198	0.451
b_8	1.049	0.874	5.821	1.359
b_9	0.0	0.009	−4.717	−0.43
b_{10}	0.0	0.57	0.007	0.007

Table 4

The values of fit parameters for equation for the pitching torque coefficient (Eq. (22)) resulting from the DNS simulations of analysed particles.

Coefficient	Ellipsoid 1	Ellipsoid 2	Disc	Fibre
c_1	2.078	0.935	3.782	0.011
c_2	0.279	0.146	0.237	−0.656
c_3	0.372	−0.469	2.351	8.909
c_4	0.018	0.145	0.236	0.396
c_5	0.98	0.116	−0.394	2.926
c_6	0.0	0.748	1.615	−1.28
c_7	0.0	0.041	−0.044	0.037
c_8	1.0	0.221	−0.537	−15.236
c_9	0.0	0.657	1.805	16.757
c_{10}	0.0	0.044	−0.037	−0.006

achieved at angles between 45° and 55°. The big improvement over literature prediction is clearly seen as the current correlations account for the effect of the Reynolds number on the lift magnitude. Presented results are however in good agreement with those obtained through Lattice Boltzmann method in [Hölzer and Sommerfeld \(2009\)](#) both in terms of shape as well as magnitude.

5.3. Pitching torque

There are two types of torque which may act on a non-spherical particle, pitching torque and rotational torque. The pitching torque occurs when the fluid flow direction is not aligned with one of the symmetry axis of the particle. The behaviour of the coefficient originating from the pitching torque can be described in the same way as in the case of the lift coefficient, as the pitching torque coefficient C_T is zero at 0° and 90°. Therefore following new equation for the pitching torque coefficient is proposed:

$$C_T = \left(\frac{c_1}{Re^{c_2}} + \frac{c_3}{Re^{c_4}} \right) \sin(\varphi)^{c_5+c_6 Re^{c_7}} \cos(\varphi)^{c_8+c_9 Re^{c_{10}}} \quad (22)$$

The parameters resulting from fitting the simulation results are given in [Table 4](#). The quality of the fit is very good for all particle shapes and flow-particle incident angles. In the case of the pitching torque coefficient, it is not straightforward to make a direct comparison with previous literature. In most articles the torque is obtained as the product of the component of the aerodynamic force, which is normal to the non-spherical particle, by the distance from centre of pressure to the centre of gravity x_{cp} :

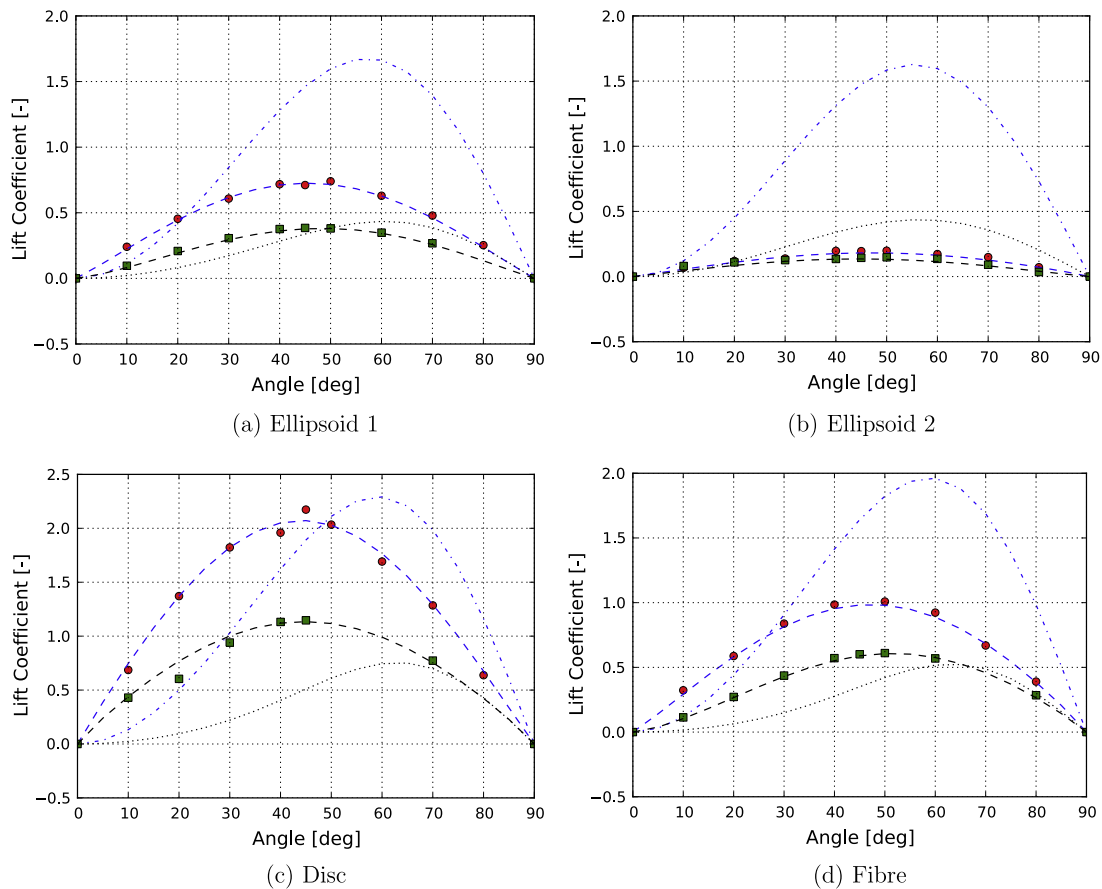


Fig. 12. Lift coefficients of the particles as a function of angle of incidence. (○) Simulation at $Re = 10$; (—) present correlation (Eq. (21)) at $Re = 10$; (---) correlation of [Hoerner \(1965\)](#) at $Re = 10$; (□) simulation at $Re = 300$; (---) present correlation (Eq. (21)) at $Re = 300$; (····) correlation of [Hoerner \(1965\)](#) at $Re = 300$. (For interpretation of the references to colour in this figure legend, the reader is referred to the web version of this article.)

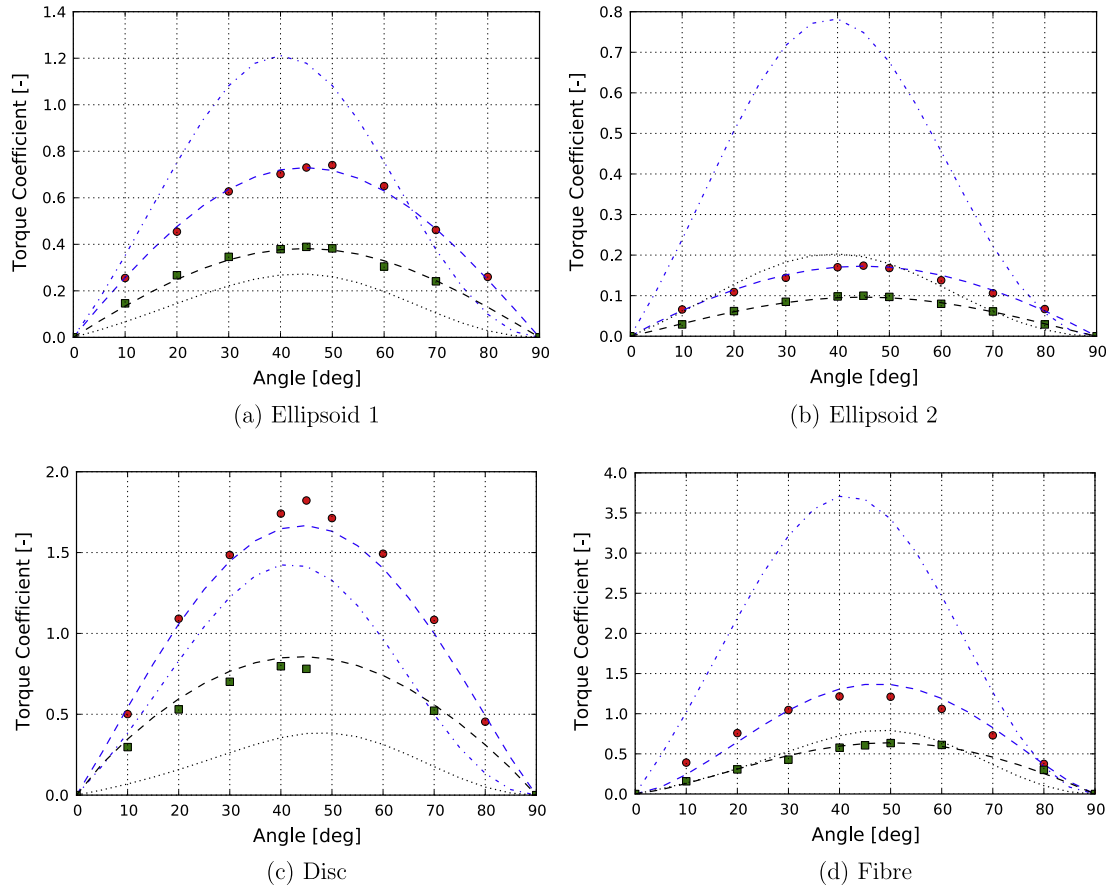


Fig. 13. Torque coefficients of the particles as a function of angle of incidence. (\circ) Simulation at $Re = 10$; (\square) simulation at $Re = 300$; (—) present correlation (Eq. (22) at $Re = 10$; (---) Eq. (23) at $Re = 10$; (---) Eq. (23) at $Re = 300$; (---) Eq. (22) at $Re = 300$. (For interpretation of the references to colour in this figure legend, the reader is referred to the web version of this article.)

$$\vec{T} = \vec{x}_{cp} \times \vec{F}_N \quad (23)$$

where the x_{cp} can be given for example by (Rosendahl, 2000):

$$x_{cp} = \frac{L}{4}(1 - \sin^3(\varphi)) \quad (24)$$

where L is the length of the non-spherical particle, while F_N is the total aerodynamic force on the non-spherical particle, with magnitude being the vector sum of the Hölzer and Sommerfeld drag (Hölzer and Sommerfeld, 2008) and the lift force predicted by the “cross flow” principle (Hoerner, 1965):

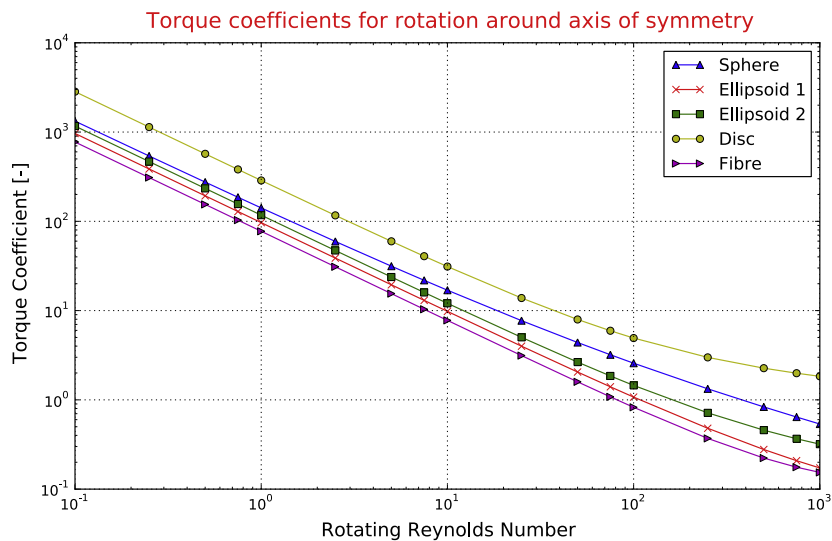


Fig. 14. Mode 1 rotational torque coefficients for the analysed particles as a function of rotational Reynolds number. Dennis et al. (1980) correlation used for the sphere.

$$F_N = \frac{\pi}{8} \rho \tilde{u}^2 d_p^2 C_D \sin(\varphi) (1 + \sin(\varphi) \cos^2(\varphi)) \quad (25)$$

The resulting torque can be transformed into the torque coefficient by using Eq. (9). The torque coefficients behaviour at various angles φ is represented in Fig. 13. The large discrepancy is the result of the fact that the errors in the lift prediction from Eq. (8) are propagated to the expression of lift (Eq. (23)), hence it is hard to evaluate the quality of the prediction of the position of the centre of pressure itself. The current results are however comparable to the torque coefficient results presented in Hölzer and Sommerfeld (2009). Therefore it can be concluded that application of Eq. (22) greatly improves the accuracy of the predictions of the torque of non-spherical particles in a fluid.

5.4. Rotational torque

The second type of torque is rotational torque, originating from the relative rotation of the particle with respect to the fluid. Simulations of rotating particles have been performed in order to determine the counter-rotational torque coefficient correlations. Two modes of rotation have been analysed: around axis of symmetry (mode 1) and around a perpendicular axis (mode 2). The fluid in the simulations is initially at rest. The particle centre of gravity is fixed at the centre of the domain, while the non-spherical particle itself is allowed to rotate with fixed angular velocity.

Fig. 14 illustrates the behaviour of the rotational torque coefficient, defined in Eq. (10), at the steady state, with changing

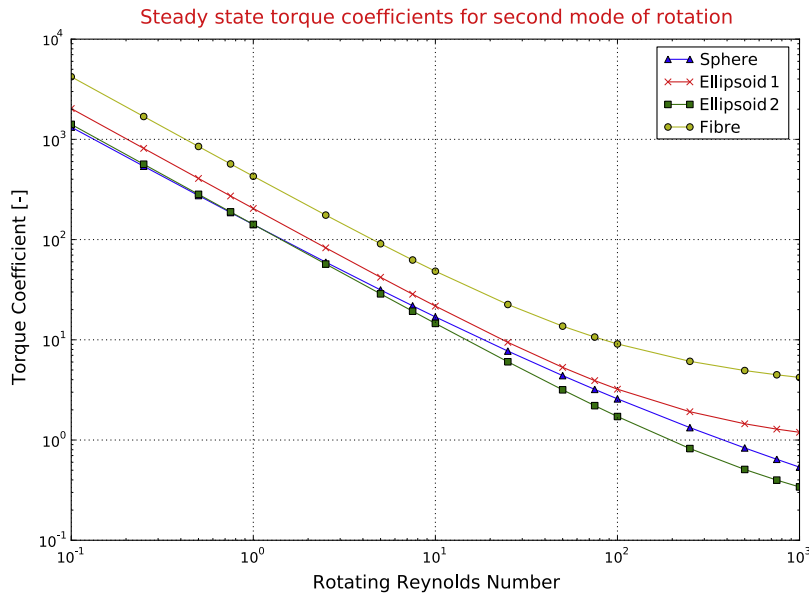


Fig. 15. Mode 2 rotational torque coefficients for analysed shapes as a function of rotational Reynolds number for a steady-state flow situation. The Dennis et al. (1980) correlation is shown for the spherical particle.

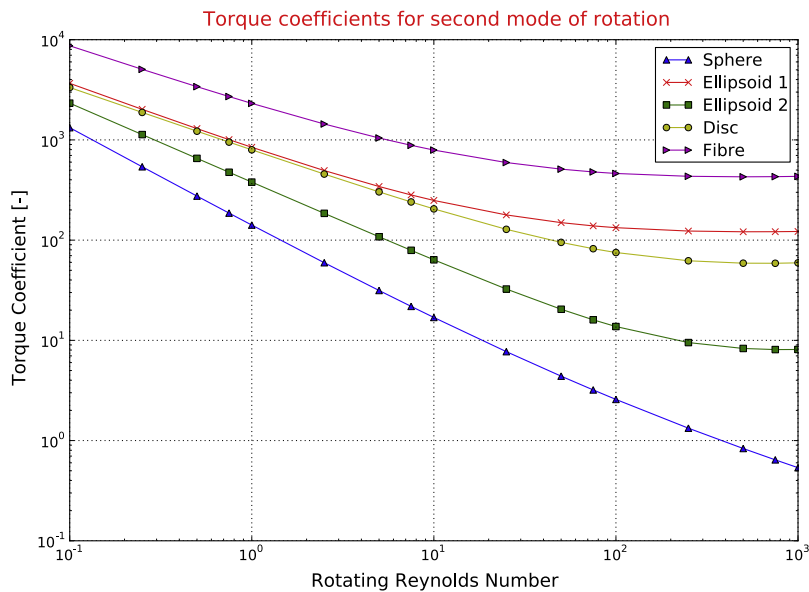


Fig. 16. Mode 2 rotational torque coefficients for analysed shapes as a function of rotational Reynolds number for the onset of rotation. The Dennis et al. (1980) correlation is for the spherical particle is shown.

rotational Reynolds number Re_R for mode 1 of rotation. The obtained values are compared to correlation for rotating spheres proposed by Dennis et al. (1980). The non-spherical particles show similar dependence on Re_R as the sphere. The magnitude of the coefficients corresponds to the cross-sectional area of particle, with disc's rotational coefficient being the highest, while fibre experiencing the smallest counter-rotational torque.

An analogous analysis can be performed for the second mode of rotation. The torque coefficients after averaging for many time-steps are shown in Fig. 15. A further analysis of the results shows that this approach is not as straightforward as in the previous case. When a spherical particle rotates around its axis of symmetry, the effective volume it occupies remains at the same position. This is, however, not the case for non-spherical bodies rotating in the second mode of rotation, as they tend to create a volume of non-steady rotating fluid, much bigger than the volume of the particle. The resulting steady torque coefficient is then not only related to the torque associated with the *initial* rotation of the particle, but with the torque associated with the particle rotation given the surrounding fluid is rotating as well. Therefore, although possible a somewhat arbitrary choice, the torque resulting from the *onset* of rotation of the particle is determined and used to determine the fit parameters.

The rotating torque coefficients resulting from the onset of rotation is presented in Fig. 16, and compared to the prediction for a rotating sphere (Dennis et al., 1980). The figure shows higher torque coefficients than those seen in Fig. 15, which is expected since in the previous case there is an established flow field around the particle. Therefore, direct comparison between results for non-spherical particles and correlation for rotating spheres given by Dennis et al. (1980) cannot be made. Particles with higher aspect ratios are subjected to larger torques with the fibre having the highest torque coefficients in a given flow situation.

Both rotation modes show similar behaviour in terms of the change in magnitude of the rotational torque coefficient with growing Re_R . Therefore they can be correlated by the following relationship, providing good data fit:

$$C_R = r_1 (Re_R)^{r_2} + \frac{r_3}{(Re_R)^{r_4}} \quad (26)$$

The specific fit coefficients for each particle type rotating around its axis of symmetry are given in Table 5, while parameters for second mode of rotation are given in Table 6.

Table 5

The values of fit parameters for equation for the rotational torque coefficient along the axis of symmetry of the particle resulting from the DNS simulations of analysed particles.

Coefficient	Ellipsoid 1	Ellipsoid 2	Disc	Fibre
r_1	0.23	0.573	3.812	0.024
r_2	−0.116	−0.154	−0.13	0.168
r_3	96.378	116.61	283.03	77.314
r_4	1.0	1.0	1.0	1.0

Table 6

The values of fit parameters for equation for the torque coefficients along the axis which are not axisymmetric of the particle resulting from the DNS simulations of analysed particles.

Coefficient	Ellipsoid 1	Ellipsoid 2	Disc	Fibre
r_1	71.03	1.244	13.31	239.76
r_2	0.069	0.239	0.189	0.075
r_3	773.04	378.12	783.05	2074.02
r_4	0.67	0.789	0.628	0.612

6. Conclusions

The behaviour of the interaction of non-spherical particles with a fluid flow is a complex phenomenon, even for axisymmetric particles in a uniform flow. Shape has a great influence on the behaviour of the particle, not only by changing the values of the experienced forces and torques but also by shifting the Reynolds number at which the transition to unsteady flow occurs. The flow field also strongly depends on the angle of incidence between the particle and the incoming fluid velocity.

Even though there have been some previous attempts to characterise the flow past an arbitrarily-shaped particle, no complete model is available. Literature provides relatively good predictions for the drag coefficient, but the predictions for both lift and torques have poor accuracy.

The present work analyses the results from a large number of true DNS of flows past various non-spherical particles at different angles of incidence and different rotation, in the range of Reynolds numbers typical for turbulent gas–solid flow. The numerical study was performed using the mirroring immersed boundary method, which allowed to obtain accurate results in an efficient way.

The analysis has resulted in newly proposed equations and fit parameters for four different non-spherical particles to predict the drag coefficient, the lift coefficient and two types of torque coefficients, which all show an excellent agreement with the DNS results. These equations predicting the force and torque coefficients can be applied to large scale simulations with many particles, to accurately elucidate their behaviour in a surrounding fluid flow field.

Acknowledgements

The authors are grateful to the Engineering and Physical Sciences Research Council (EPSRC) for their financial support (Grant No. EP/G049262/1) and the Jan Dzienisiewicz trust for providing M. Zastawny with a bursary.

References

- Besnard, D., Harlow, F., 1986. Nonspherical particles in two-phase flow. *International Journal of Multiphase Flow* 12, 891–912.
- Brenner, H., 1963. The stokes resistance of an arbitrary particle. *Chemical Engineering Science* 18, 1–25.
- Cherukat, P., McLaughlin, J., Dandy, D., 1999. A computational study of the inertial lift on a sphere in a linear shear flow field. *International Journal of Multiphase Flow* 25, 15–33.
- Chhabra, R., Agarwal, L., Sinha, N., 1999. Drag on non-spherical particles: an evaluation of available methods. *Powder Technology* 101, 288–295.
- Crowe, C.T. (Ed.), 2006. *Multiphase Flow Handbook*. Taylor and Francis Group, LLC, USA.
- Dennis, S.C.R., Singh, S.N., Ingham, D.B., 1980. The steady flow due to a rotating sphere at low and moderate Reynolds numbers. *Journal of Fluid Mechanics* 101, 257–279.
- Ergun, S., 1952. Fluid flow through packed columns. *Chemical Engineering Progress* 48, 89–94.
- Gallily, I., Cohen, A.H., 1979. On the orderly nature of the motion of nonspherical aerosol particles: II. Inertial collision between a spherical large droplet and an axially symmetrical elongated particle. *Journal of Colloid and Interface Science* 68, 338–356.
- Ganser, G., 1993. A rational approach to drag prediction of spherical and nonspherical particles. *Powder Technology* 77, 143–152.
- Haider, A., Levenspiel, O., 1989. Drag coefficient and terminal velocity of spherical and nonspherical particles. *Powder Technology* 58, 63–70.
- Hartman, M., Trnka, O., Svoboda, K., 1994. Free settling of nonspherical particles. *Industrial & Engineering Chemistry Research* 33, 1979–1983.
- Hoerner, J., 1965. Fluid-dynamics drag. *Hoerner Fluid Dynamics*.
- Hölzer, A., Sommerfeld, M., 2008. New simple correlation formula for the drag coefficient of non-spherical particles. *Powder Technology* 184, 361–365.
- Hölzer, A., Sommerfeld, M., 2009. Lattice boltzmann simulations to determine drag, lift and torque acting on non-spherical particles. *Computers and Fluids* 38, 572–589.
- Hu, H., 1996. Direct simulation of flows of solid-liquid mixtures. *International Journal of Multiphase Flow* 22, 335–352.
- Jeffery, G.B., 1922. The motion of ellipsoidal particles immersed in a viscous fluid. *Proceedings of the Royal Society of London. Series A, Containing Papers of a Mathematical and Physical Character* 102, 161–179.

- Kunii, D., Levenspiel, O., 1991. *Fluidization Engineering*, second ed. Butterworth-Heinemann.
- Kurose, R.K.S., 1999. Drag and lift forces on a rotating sphere in a linear shear flow. *Journal of Fluid Mechanics* 384, 183–206.
- Lazaro, B.J., Lasheras, J., 1989. Particle dispersion in turbulent, plane, free shear layer. *Physics of Fluids A* 1, 1035–1044.
- Loth, E., 2008a. Drag of non-spherical solids particles of regular and irregular shape. *Powder Technology* 182, 342–353.
- Loth, E., 2008b. List of a solid spherical particle subject to vorticity and/or spin. *AIAA Journal* 46, 801–809.
- Mando, M., Rosendahl, L., 2010. On the motion of non-spherical particles at high Reynolds number. *Powder Technology* 202, 1–13.
- Marchioli, C., Fantoni, M., Soldati, A., 2010. Orientation, distribution, and deposition of elongated, inertial fibers in turbulent channel flow. *Physics of Fluids* 22, 033301.
- Mark, A., van Wachem, B., 2008. Derivation and validation of a novel implicit second-order accurate immersed boundary method. *Journal of Computational Physics* 227, 6660–6680.
- Mohd-Yusof, J., 1997. Combined immersed-boundary/B-spline methods for simulations of flow in complex geometries. Technical Report. Center for Turbulence Research, Annual Research Briefs.
- Mortensen, P.H., Andersson, H.I., Gillissen, J.J.J., Boersma, B.J., 2008. Dynamics of prolate ellipsoidal particles in a turbulent channel flow. *Physics of Fluids* 20, 093302.
- Niazmand, G., Renksizbulut, R., 2003. Surface effects on transient three-dimensional flows around rotating spheres at moderate Reynolds numbers. *Computers & Fluids* 32, 1405–1433.
- Peskin, C., 1977. Numerical analysis of blood flow in the heart. *Journal of Computational Physics* 25, 220–252.
- Rosendahl, L., 2000. Using a multi-parameter particle shape description to predict the motion of non-spherical particle shapes in swirling flow. *Applied Mathematical Modelling* 24, 11–25.
- Rubinow, S., Keller, J., 1961. The transverse force on a spinning sphere moving in a viscous fluid. *Journal of Fluid Mechanics* 11, 447–459.
- Schiller, L., Naumann, A., 1933. Über die grundlegenden berechnungen bei der schwerkraftaufbereitung. *Zeitschrift des Vereines Deutscher Ingenieure* 77, 318–320.
- van Wachem, B., Oliveira, J., Zastawny, M., 2010. A novel immersed boundary method for interacting particles. In: 7th International Conference on Multiphase Flow (ICMF2010), Tampa, Florida, USA, May 30–June 4.
- Wadell, H., 1934. The coefficient of resistance as a function of Reynolds number for solids of various shapes. *Journal of the Franklin Institute* 217, 459–490.
- Wen, C.Y., Yu, Y.H., 1966. *Mechanics of fluidization*. Chemical Engineering Progress Symposium Series 62, 100–111.
- Yin, C., Rosendahl, L., Kaer, S., Soerensen, H., 2003. Modelling the motion of cylindrical particles in a nonuniform flow. *Chemical Engineering Science* 58, 3489–3498.